# Chitosan-Coated Superparamagnetic Fe 3 O 4 Nanoparticles for Magnetic Resonance Imaging, Magnetic Hyperthermia, and Drug Delivery

Jules Mistral, Kevin Tse Ve Koon, Luiz Fernando Cotica, Gustavo Sanguino Dias, Ivair Aparecido Santos, Pierre Alcouffe, Nadège Milhau, Didier Pin, Olivier Chapet, Anatoli Serghei, et al.

ACS APPLIED NANO MATERIALS

www.acsanm.org Article

# Chitosan-Coated Superparamagnetic $Fe_3O_4$ Nanoparticles for Magnetic Resonance Imaging, Magnetic Hyperthermia, and Drug Delivery

Jules Mistral, Kevin Tse Ve Koon, Luiz Fernando Cotica, Gustavo Sanguino Dias, Ivair Aparecido Santos, Pierre Alcouffe, Nadège Milhau, Didier Pin, Olivier Chapet, Anatoli Serghei, Guillaume Sudre, Catherine Ladavière, Paula Nunes De Oliveira,* and Laurent David*

Cite This: https://doi.org/10.1021/acsanm.3c06118 Read Online

ACCESS | Metrics & More | Article Recommendations | Supporting Information

**ABSTRACT:** Superparamagnetic iron oxide nanoparticles (SPIONs) have great potential for biomedical applications as multipurpose magnetic resonance imaging (MRI) contrast agents, and some systems have already been approved by The United States Food and Drug Administration for clinical use. Superparamagnetic behavior, high magnetic saturation, and fast synthesis are the major advantages of these nanomaterials. Polymer coatings are often used to prevent cluster formation and to improve biocompatibility of nanoparticles. In this work, we propose to use chitosan (CS) coatings as a means to tune the biocompatibility and magnetic properties of the SPIONs. For this purpose, magnetite ($Fe_3O_4$) SPIONs with various CS coatings were synthesized. CS with identical degree of polymerization (DPw = 450) but different degrees of acetylation (DA of 1, 14, and 34%) were employed to tune the hydrophilic properties of the SPIONs' coatings. A highly crystalline magnetite phase with a superparamagnetic behavior was evidenced for all the studied nanoparticles, whose average sizes varied between 5 and 10 nm. Adjusting the preparation process enabled us to control precisely the amount of coating on the SPIONs. Such coatings significantly impacted their magnetic properties, which were found to decrease with the quantity of CS and also with its DA. Interestingly, cytocompatibility was enhanced by the presence of the CS coating so that all CS-coated SPIONs studied were found to be nontoxic, independently of the coating amount. This trade-off approach suggests that optimal SPIONs systems would consist of a magnetite core, coated with a low amount of low-DA CS. Finally, the multimodal features of the SPIONs were evidenced by performing magnetic hyperthermia and MRI measurements. Despite significant differences, for all the CS-coated SPIONs, the magnetic properties remained strong enough to envision their use in various biomedical applications such as magnetic hyperthermia, MRI contrast agents, magnetic field-assisted drug delivery, and as platforms for further biological functionalization.

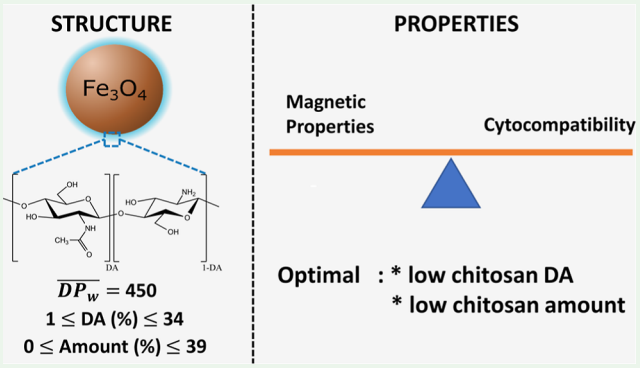


**KEYWORDS:** *magnetic nanoparticles, chitosan, hyperthermia, MRI, cytotoxicity, nanomedicine*

## 1. INTRODUCTION

Superparamagnetic iron oxide nanoparticles (SPIONs) can be used for a variety of biomedical applications including carrier for drug delivery, magnetic hyperthermia for cancer treatment or as magnetic resonance imaging (MRI) contrast agents.[1−3] Among SPIONs, magnetite ($Fe_3O_4$) and maghemite ($\gamma$-$Fe_2O_3$) have been widely studied due to their good magnetic properties and low toxicity.[4] Magnetite has a cubic inverse spinel structure (space group $Fd3m$), with oxygen ions in a cubic packed arrangement that contains both divalent Fe(II) and trivalent Fe(III) ions, with an ideal ratio of Fe(III)/Fe(II) = 2. The Fe(II) ions occupy half of the octahedral sites, while the Fe(III) ions are evenly split between the other half of the octahedral and tetrahedral sites.[5] The magnetic property of iron oxide nanoparticles depends on their crystalline phase, but it is well-known that superparamagnetism is observed for SPIONs with sizes below ∼20 nm. Thus, at ambient temperature and in the absence of magnetic field, the magnetic potential energy that governs the direction of the spontaneous magnetization is lower than the thermal bath energy,[6] resulting in zero net magnetic moment. The size and shape of magnetite nanoparticles are key properties for biomedical applications as they directly impact their magnetic and biological properties.[7,8]

Received: December 21, 2023
Revised: February 21, 2024
Accepted: February 29, 2024

The superparamagnetic behavior of $Fe_3O_4$ SPIONs is thus characterized by almost zero coercivity and no hysteresis. When injected in the body, this type of SPIONs present a magnetic moment only under the presence of an external magnetic field and reach saturation magnetization ($M_s$) orders of magnitude above that of biological components. The SPIONs can therefore be detected and manipulated in the body, making superparamagnetism property the basis for biomedical applications.[9]

Among the methods to synthesize $Fe_3O_4$ SPIONs, the coprecipitation is the most employed route as it is quick, simple, and effective.[10] This method consists in mixing of iron ions in an acidic solution in the absence of oxygen (under an argon inert atmosphere) to prevent their oxidation and the formation of hematite ($\alpha$-$Fe_2O_3$), which has no (or very weak) magnetic response. Then, the pH is increased by the addition of a basic solution, leading to the formation of ferrous and ferric hydroxides and then to the precipitation of magnetite $Fe_3O_4$ SPIONs.[11]

However, bare magnetite SPIONs may have cytotoxic effects.[12,13] Thus, in order to address a variety of biomedical applications, SPIONs are usually coated to improve their colloidal stability and their biocompatibility.[14] Such coated particles are usually referred to as "core−shell" SPIONs.[15] Many types of shells have been reported. Among them, metals such as silver and gold have been widely studied,[16,17] as well as silica, titanium, or zinc-based oxides.[18−20] Also, synthetic polymers like poly(ethylene glycol) (PEG) or natural polysaccharides such as alginate and dextran have been extensively used.[21−23] Overall, coating addition was found to drastically improve the biological properties compared to those of bare SPIONs, so that a coating is systematically present on all $Fe_3O_4$ SPION-based medical devices approved worldwide.[24,25] However, despite the improvement of the biological properties, the coatings have also been reported to dramatically decrease the magnetic properties of SPIONs, regardless of the coating type.[26−29] Therefore, a biocompatibility/magnetic property trade-off needs to be found, certainly depending on the desired applications.

Among the various possibilities of polymer coatings for the SPIONs, chitosan (CS) and CS derivatives were investigated in several previous works.[30−32] Indeed, CS has many interesting properties, such as to be biocompatible, biodegradable, antibacterial, and nontoxic[33] Also, CS has reactive amine and hydroxyl sites, which allow its complexation with metals. However, these studies very often adopt a focused scope, evaluating one given type of CS-coated SPION designed for a specific application and particular evaluation conditions.[34,35] Thus, the impact of CS coating parameters such as degree of acetylation (DA) and weight percentage is rarely addressed. Finally, CS polymers are not always fully characterized (e.g., in terms of molar mass distributions).

In a previous work of our group,[36] we synthesized $Fe_3O_4$ SPIONs coated with CS oligosaccharides (COS) with controlled DA and degree of polymerization. We evidenced a narrow size distribution, high magnetic saturation ($M_s$), and low cytotoxicity of these COS-coated SPIONs. However, COS may be difficult to prepare and characterize. Therefore, we choose here to use longer CS chains as coating materials. In this new work, we addressed the problematic competition between the biological and magnetic properties of core−shell SPIONs, using $Fe_3O_4$ as core and tuned amounts of fully characterized and comparable CS polymers as shells, with such SPIONs being synthesized and coated in aqueous conditions without use of cross-linkers. In a systematic study of SPIONs' physicochemical, magnetic, and biological properties, we deeply investigated the influence of CS coatings' characteristics on SPIONs' efficacy and relevancy for MRI and magnetic hyperthermia (MH) applications. Besides, a wide range of experimental configurations were explored, with MRI measurements on five devices with field strengths ranging from 0.5 to 11.7 T, and MH experiments at three different field amplitudes (100−370 G) and frequencies (168−491 kHz). This in-depth study generated a wide range of converging data, which clearly indicated the existence of an optimal DA and weight percentage for CS coating in order to guarantee excellent magnetic and biological SPION properties. Additionally, this work highlighted the multifunctional features of these CS-coated SPIONs, allowing to envision their use for MRI, MH, and drug delivery applications, as well as platforms for theragnostics and biofunctionalization tools.

## 2. EXPERIMENTAL SECTION

**2.1. Materials.** Commercial CS from shrimp shells (batch type 244/020208; DA < 1%; $M_w$ = 186 kg/mol; $M_n$ = 97 kg/mol; $D$ = 1.9), was bought from Mahtani Chitosan Pvt. Ldt (Veraval, India) and characterized by proton nuclear magnetic resonance ($^1$H NMR)[37] and Size-exclusion chromatography−multi angle laser-light scattering (SEC-MALLS).[38] Iron(III) chloride hexahydrate ($FeCl_3{\cdot}6H_2O$), iron(II) chloride tetrahydrate ($FeCl_2{\cdot}4H_2O$), hydrochloric acid (37%), acetic acid, aqueous ammonia (28%), propylene glycol, ammonium acetate, and sodium nitrite were purchased from Sigma-Aldrich. Extra-pure pork gelatin (platinum, 240 bloom) was purchased from Roth.

**2.2. CSs and $Fe_3O_4$ SPION Syntheses.** *2.2.1. Depolymerization of CS.* A controlled depolymerization of the initial 244 CS was performed. For that, a CS solution at a concentration of 0.5% (w/v) was prepared using 20 g of CS 244 and 4 L of a 0,2 M acetic acid/0,15 M ammonium acetate buffer (pH = 4,5). The mix was mechanically stirred for 24 h to ensure the complete solubilization of CS. A filtration under pressure was performed to remove insolubles. The solution was filtered twice, using consecutive filters (Millipore) of 3 and 1.2 $\mu$m pore size. Once purified, the CS solution was placed under mechanical stirring, and the depolymerization process was initiated by adding 77 mL of a sodium nitrite solution at 1 mg/mL in order to reach a stoichiometric ratio $n_{nitrito}/n_{glucosamine}$ of 0.1. According to pre-established depolymerization curves,[39] the reaction time was set to 55 min. The reaction was stopped by the addition of ammonium hydroxide until reaching a basic pH (~10−11) to precipitate CS. The obtained CS was washed and centrifuged several times until reaching neutral pH (~6.3). Finally, CS was freeze-dried.

*2.2.2. Reacetylation of CS.* A homogeneous series of CSs with different DAs was prepared.[40] To this end, two reacetylations yielding DAs of 14 and 34% were performed starting from the previously described depolymerized CS ($CS_1$). These reacetylations were performed following a method described elsewhere.[41] Briefly, 6 g of $CS_1$ was diluted for each case in 480 mL of a water/propylene glycol mixture (50/50 v/v) with acetic acid at a concentration of 3.3 g/L. Then, given amounts of acetic anhydride diluted in propylene glycol were added dropwise to reach DAs of 14 and 34%, and solutions were stirred overnight. At last, CSs were precipitated by addition of ammonium hydroxide until pH ranged 10−11. CSs were washed by successive centrifugations (10 min, 10,000 rpm) and dilutions with deionized water several times to remove all propylene glycol and reach a neutral pH. Finally, CSs were then freeze-dried.

*2.2.3. Synthesis of $Fe_3O_4$ SPIONs.* The synthesis of $Fe_3O_4$ SPIONs was achieved by chemical coprecipitation method. The advantage of this technique is its simplicity and high production yield, but other processing methods such as flame spray pyrolysis[42] and electrochemical method are also scalable. Thus, iron(III) chloride hexahydrate ($FeCl_3{\cdot}6H_2O$) and iron(II) chloride tetrahydrate


https://doi.org/10.1021/acsanm.3c06118
ACS Appl. Nano Mater. XXXX, XXX, XXX−XXX

($FeCl_2{\cdot}4H_2O$) were dissolved at a stoichiometric ratio of 2:1 in deionized water at 60 °C under an inert atmosphere (Ar). HCl was added to the mixture to reach the concentration of 0.1 M and stabilize the iron ions. Precipitation of iron ions to form magnetite was achieved by dropwise addition of $NH_4OH$ to reach a pH in the range ∼10−11. The formation of magnetite by chemical precipitation could be clearly evidenced by the immediate change of color of the solution from yellow to black upon addition of $NH_4OH$. Then, the SPIONs were washed several times with deionized water and collected using magnetic decantation until reaching neutral pH. They were finally freeze-dried and stored at room temperature.

*2.2.4. Synthesis of $Fe_3O_4$ SPIONs Coated with CS.* Synthesis of $Fe_3O_4$ SPIONs coated with CS of various DA ($Fe_3O_4/CS_{DA}$) was carried out through the same chemical coprecipitation method in the presence of solubilized CS. First, 50 mL of CS solution at a concentration of 2.5 g/L was prepared in an aqueous acidic medium (HCl). For CS of DA 1%, solutions were prepared at different concentrations depending on the desired amount of CS on SPIONs (see Table S1). 0.905 g of $FeCl_3{\cdot}6H_2O$ and 0.333 g of $FeCl_2{\cdot}4H_2O$ were dissolved in 20 mL of water at 60 °C under an inert atmosphere and mechanical stirring, followed by the addition of HCl for ion stabilization. Then, CS solution was added slowly to the iron salts solution. After 1 h, stirring was increased, and $NH_4OH$ was added dropwise to the solution to increase the pH (∼10−11) and therefore to precipitate the CS-coated $Fe_3O_4$ SPIONs. The obtained CS-coated SPIONs were washed in deionized water and separated by magnetic decantation until the pH became neutral. Finally, SPIONs were freeze-dried and stored at room temperature. The same synthesis route was repeated to obtain CS-coated $Fe_3O_4$ SPIONs with the reacetylated CSs analyzed in this work, and its principle is illustrated in Scheme 1 below.

**Scheme 1. Synthesis Principle of $Fe_3O_4/CS_{DA}$ SPIONs from a CS Acetate Solution Including Fe(II) and Fe(III) Ions[a]**

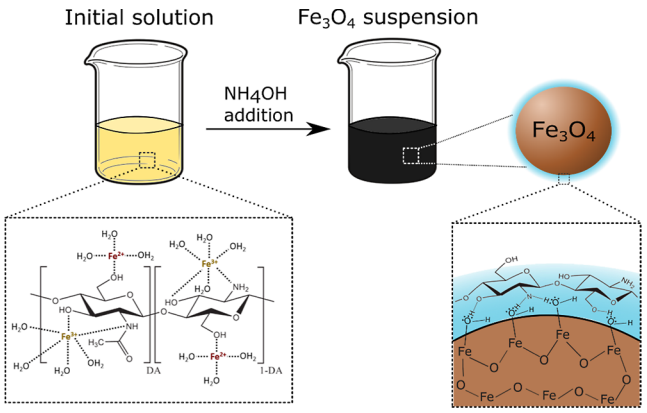


[a]Precipitation under inert gas is induced by pH increase in the presence of ammonia and results in CS-coated nanoparticles.

**2.3. Materials' Characterization.** *2.3.1. Determination of the DA of CSs.* Depolymerized (low DA) and reacetylated CSs were characterized using $^1H$ NMR in order to determine more precisely their respective DAs.[37] Samples were prepared by dissolving 10 mg of CS in 1 mL of $D_2O$ with 5 μL of HCl (12 N). The solutions were then transferred to NMR tubes. Analyses were carried out at room temperature using a 400 MHz spectrometer (Bruker). Trimethylsilyl-3-propionic-2,2,3,3-$d_4$ acid sodium salt was used as an internal reference.

*2.3.2. Analysis of CS Average Molar Mass.* SEC was performed to analyze both depolymerized and reacetylated CSs. First, CS was dissolved overnight at 1 mg/mL in 0.2 M AcOH/$AcONH_4$ 0.15 M buffer. The solution was then filtered through cellulose methyl ester membranes with 0.22 μm pore size and put in an SEC vial. The analyses were done with a system comprising a 1260 infinity pump (Agilent technology) connected to two columns, TSKgel G2500PW and G6000PW (Tosoh Bioscience). The MALLS detector used was a Dawn Heleos II (Wyatt) operating at 690 nm and coupled to an Optilab T-Rex refractometer (Wyatt). The refraction index increments were selected according to the values of DA.[38]

*2.3.3. FTIR Analysis of CS-Coated SPIONs.* Samples were mixed with KBr and pressed to form pellets. Infrared spectra were recorded with a Nicolet iS-10 FTIR spectrometer (Thermo Scientific). The range of analysis was 4000−400 $cm^{-1}$. For each measurement, 200 scans were performed with a resolution of 4 $cm^{-1}$.

*2.3.4. Determination of Organic Coating Amount on SPIONs.* Analyses were carried out with a TGA Q-500 device (TA Instruments). Thermograms were recorded from 30 to 700 °C with a heating rate of 10 °C/min under dry air. Sample mass loss above 200 °C was used to determine the amount of CS on the SPIONs.

*2.3.5. Size Distributions of SPIONs.* SPIONs were observed by transmission electron microscopy (TEM) (at the Centre Technologique des Microstructures CTμ, Villeurbanne, France). Suspensions were prepared in deionized water for both "pristine" $Fe_3O_4$ SPIONs and for CS-coated SPIONs and were sonicated for 15 min. Then, one droplet of each suspension was put on separated ultrafine carbon TEM grids, and the solvent was evaporated at room temperature. Images of nanoparticles were obtained using a 1400 flash (JEOL) microscope equipped with a camera Rio 16 (Gatan). For each sample, size distribution was obtained by measuring the diameter of 250 SPIONs using ImageJ program and by fitting the data with a log-normal distribution function.

*2.3.6. Analysis of the Crystalline Structure of SPIONs.* Wide-angle X-ray scattering (WAXS) experiments were performed at European Synchrotron Radiation Facility (ESRF) (Grenoble, France), on D2AM beamline. SPIONs were placed on a homemade sample holder and entrapped between two Kapton tapes. The incident photon energy was set to 15.7 keV, with a beam diameter of 45 μm. A WAXS Open for SAXS (WOS) 2D-detector was used, from IMXPAD.[43] The distance between the sample and the detector was set to ∼10 cm. The scattering vector $q$ calibration was performed using a chromium oxide ($Cr_2O_3$) powder reference. All scattered images were normalized by the transmitted intensity, and azimuthal averages were calculated around the image center (mean center of incident beam). The signal corresponding to an empty cell with only 2 Kapton tapes was recorded and subtracted of each sample in order to obtain the scattering diagram of the samples. The estimation of crystallite size was done using the isotropic Williamson−Hall model,[44] corresponding to the following equation

$$\beta_{hkl}\cos(\theta_{hkl}) = \frac{k\lambda}{D} + 4\varepsilon\sin(\theta_{hkl}) \quad (1)$$

where $\beta_{hkl}$ is the full width at half-maximum (fwhm) of the diffraction peak corresponding to the ($hkl$) family of reticular planes. $\beta_{hkl}$ was determined using a fitting of the scattering profile with Voigt function (combination of Gauss and Lorentz fittings) for (220), (311), (400), (511), and (440) diffraction peaks. $\theta_{hkl}$ is the Bragg angle (in radians) corresponding to the ($hkl$) diffraction peak, $k$ is a constant ($k \sim 0.9$ for isometric crystals), $\lambda$ is the wavelength of the incident radiation ($\lambda$ = 0.7907 Å), $D$ is the average crystallite size of the sample, and $\varepsilon$ is the lattice strain. A linear fit was performed to extract the crystallite size of each sample.

*2.3.7. Analysis of SPIONs Suspensions.* Small-angle X-ray scattering (SAXS) experiments were also performed at ESRF on D2AM beamline using the same beam in the conditions of simultaneous SAXS/WAXS experiments. SPION suspensions were prepared at 1 mg/mL in ultrapure water for $Fe_3O_4$ and in ultrapure water + 1 μL/mL of pure acetic acid for CS-coated $Fe_3O_4$ SPIONs in order to facilitate their redispersion from powders. The suspensions were sonicated during 40 min and then transferred in glass tubes (Deutero GmbH, ref 600020-200, external diameter: 3 mm, length: 60 mm, width: 0.2 mm). The sample to detector distance was set to 1.89 m. D5 solid state detector (IMXPAD) was used for the 2D image collection. Again, the $q$-range calibration was performed with a standard (silver behenate), the scattering diagrams were normalized


https://doi.org/10.1021/acsanm.3c06118
ACS Appl. Nano Mater. XXXX, XXX, XXX−XXX

by transmission, and the signal of the empty cell (solvent + tube) was subtracted in order to deduce the SPIONs' signal at small angles.

*2.3.8. Magnetization Measurements.* The magnetic curves were determined at room temperature, under an applied magnetic field ranging from −10 to 10 kOe, using a vibrating sample magnetometer (VSM). The magnetic measurements as a function of temperature have been carried out in a Cryomagnetics ModelC—Mag Vari-9T Research System. Temperature-dependent magnetization $M$ was measured in the zero-field-cooling (ZFC) and field-cooled (FC) regimes. In ZFC protocol, the sample was cooled down to the lowest temperature (4 K) in the absence of any external magnetic field ($H$). At $T$ = 4 K, the measurement field (100 Oe) was applied, and $M \times T$ curve was recorded during warming. After recording $M$ in the ZFC mode, the sample was subsequently cooled down until $T$ = 4 K at the same field and temperature dependence. The temperature sweep rate during the measurements of $M$ was 1 K/min.

*2.3.9. MH Measurements.* For each measurement, 1 mL of suspension at a concentration of 5 mg/mL was prepared. Samples were then sonicated for 15 min. D5 series thermomagnetometer (Nanoscale Biomagnetics) equipped with a G2 Driver and a cal 2 coil (Nanoscale Biomagnetics) was used for the measurements. We investigated three different frequencies (491, 306, and 168 kHz) and magnetic field amplitudes (370, 200, and 100 G) for each sample. Temperature was initially stabilized at ∼25 °C, followed by 10 min of acquisition at fixed field amplitude and frequency. The obtained temperature vs time curves were used to determine the specific absorption rate (SAR) value of the SPIONs, according to

$$\mathrm{SAR} = C_{\mathrm{p-solvent}} \frac{\Delta T/\Delta t}{C_{\mathrm{Fe}}} \quad (2)$$

where $C_{\mathrm{p\text{-}solvent}}$ is the specific heat capacity of the solvent (4.186 J $K^{-1}$ $g^{-1}$ for water), $\Delta T/\Delta t$ is the initial temperature rate in °C/s, and $C_{\mathrm{Fe}}$ is the concentration of iron oxide in g/mL. In this work, $\Delta T/\Delta t$ was calculated considering a time range between 0 and 60 s.

*2.3.10. MRI Analyses.* SPIONs were first embedded in gelatin hydrogels to prevent any movement or aggregation during the experiment. Briefly, gelatin was dissolved in water (3% m/v) under mechanical stirring at 80 °C. Then, 4 mL of the gelatin solution and 0.5 mL of a SPIONs suspension at a given concentration were introduced in 5 mL glass tubes (180 × 7.5 × 0.6 mm). The concentration of the SPION suspension was adjusted depending on the final concentration needed in the hydrogel. The tubes containing gelatin + SPIONs suspension were manually stirred to obtain a homogeneous mixture and then placed in the fridge overnight for gelation. MRI experiments were conducted at CREATIS Laboratory (Villeurbanne, France) for 11.7 and 7 T using Bruker Biospec MR scanners and at 0.5 T using a Pure Devices benchtop MRI. 3 T acquisitions were carried out at Léon Bérard center (Lyon, France) on a Siemens Syngo MRI scanner and at Hospital Lyon Sud (Pierre-Bénite, France) for 1.5 T using an Elekta Unity MRI scanner. For $T_1$ acquisitions, saturation-recovery sequences were used at 0.5, 1.5, 7, and 11.7 T, while modified look-locker imaging (MOLLI) sequence was employed at 3 T. For $T_2$ acquisitions, multiecho spin−echo sequences were used for all analyses.

*2.3.11. Cytotoxicity Analysis.* Canine dermal fibroblasts were isolated from a dead neonatal dog obtained from VetAgro Sup—Campus Vétérinaire de Lyon (Marcy l'Etoile, France) in accordance with the VetAgro Sup animal ethics committee. Skin specimens were collected from the abdominal surface of the dog, cut into small fragments, and digested with 0.25% trypsin/ethylenediaminetetraacetic acid (EDTA) (Eurobio, France) for 15 min at 37 °C. After digestion, the skin fragments were washed with phosphate-buffered saline (PBS). Dermal fibroblast cultures were established by explant culture in 25 $cm^2$ flasks (Falcon, VWR international, France) containing Dulbecco's modified Eagle's medium (Eurobio, France) supplemented with 20% fetal calf serum, 2 mM L-glutamine, and 2% penicillin/streptomycin/amphotericin B (Eurobio, France) at 37 °C in a humidified atmosphere with 5% $CO_2$. After 2 days, the fibroblasts started to grow out, and fragments were removed. After 5 days, the cells reached confluence and were subcultured after 0.25% trypsin/EDTA treatment in 75 $cm^2$ flasks (Falcon, VWR international, France). The culture medium was changed two times a week. Cells are used between three and six passages.

Cell viability was investigated in accordance with the international standard operation procedure "Tests for in vitro cytotoxicity" ISO 10993-5. Cell cytotoxicity was assessed by the CCK-8 assay (Sigma-Aldrich, France) according to the manufacturer's instructions. This assay is based on reduction of soluble yellow tetrazolium into insoluble purple formazan crystals by mitochondrial succinate dehydrogenase of viable cell. Therefore, the rate of formazan crystal formation is directly proportional to number of viable cells, which is measured in terms of absorbance. For this, canine fibroblasts were seeded at a density of 1 × $10^4$ cells/well in 96-well plate at 37 °C in humidified atmosphere with 5% $CO_2$. After 2 days of culture, the medium was replaced with fresh medium containing $Fe_3O_4$ nanoparticle formulations with concentrations of 0 [control], 0.060, 0.125, 0.250, 0.500, and 1 mg/mL. Three exposure times (24, 48, and 72 h) were tested in all experiments. After incubation, 10 μL CCK8 was added into each well and incubated at 37 °C for 2 h. The absorbance was measured at 450 nm using a microplate reader (MultiSkan, Thermo Fisher). Cell viability was determined as the ratio of the optical density (OD) of exposed cells to the OD of the untreated cells ×100. For each concentration of nanoparticles, mean values of the mean absorbance rates from eight wells were calculated, and results were expressed as mean ± standard deviation. All experiments were performed in duplicate. Graphs and statistical analyses (Tukey test) were performed using Origin software. $P$-values ≤0.05 were considered significant.

## 3. RESULTS AND DISCUSSION

**3.1. Coating Analysis of SPIONs.** *3.1.1. In-Depth CS Average Molar Weight Characterization.* Table S2 gathers the macromolecular characterizations of different CSs that were prepared and used in this work. As expected, a decrease of $M_w$ was observed from initial CS to $CS_1$, which underwent a depolymerization process and was further used for the preparation of $CS_{14}$ and $CS_{34}$. The depolymerization by nitrous deamination also contributed to narrow the molar weight distributions, with a significant decrease of dispersity $Đ$. The average DA was determined by $^1$H NMR, with DAs for $CS_{14}$ and $CS_{34}$ close to the targeted values. This reacetylation induced an increase in the average molar weights, but the value of the mean degree of polymerization was quite constant. Thus, $CS_1$, $CS_{14}$, and $CS_{34}$ constitute a homologous series of statistical CSs. Details about calculations can be found in the Supporting Information and chromatograms in SI2.

*3.1.2. CS−Magnetite Nanoparticle Interactions Studied by Vibrational Spectroscopy (FTIR).* Figure S3a shows the Fourier transform infrared (FTIR) spectra of CSs with different DAs ($CS_{DA}$). Several characteristic bands of CS were identified.[45] The bands in the range of 3600−3000 $cm^{-1}$ were attributed to axial stretching of O−H and N−H bounds. Absorption bands at 2930 and 2875 $cm^{-1}$ indicated C−H axial stretching of $CH_2$ and $CH_3$ groups, respectively. For $CS_1$, the absorption band at 1600 $cm^{-1}$ was attributed to the angular deformation of N−H in amine groups ($-NH_2$). Some differences were observed for $CS_{14}$ and $CS_{34}$ due to different DA, with bands at 1660 and 1550 $cm^{-1}$ indicating, respectively, C═O axial stretch and angular deformation of N−H bonds for amino groups. As expected, the relative intensity of the C═O band increases with DA, evidencing the effective reacetylation of CS. For all $CS_{DA}$, coupling of C−H angular deformation and C−N axial stretching were found at 1380 and 1420 $cm^{-1}$. Finally, the vibration bands for the polysaccharide skeleton evidencing C−O and C−O−C stretching were found in the


https://doi.org/10.1021/acsanm.3c06118
ACS Appl. Nano Mater. XXXX, XXX, XXX−XXX

range [1150−900 $cm^{-1}$].[46] Figure S3b shows IR spectra for noncoated and coated $Fe_3O_4$ SPIONs. The absorption bands of $Fe_3O_4$ SPIONs appeared at 590 and 440 $cm^{-1}$. These bands are shifted in comparison to those of bulk magnetite, with absorption bands at 570 and 375 $cm^{-1}$, respectively.[47] This change may be attributed to nano-size effects of the SPIONs. The Fe−O bonds close to the surface are bended and distorted, therefore they vibrate at higher wavenumbers than that in bulk magnetite, where the bonds are not physically constrained. In comparison to noncoated $Fe_3O_4$ SPIONs, the FTIR spectra of $Fe_3O_4/CS_{DA}$ SPIONs show the characteristic absorption bands of magnetite at 590 and 440 $cm^{-1}$, but the typical bands of CS were also present and appeared slightly shifted. For $Fe_3O_4/CS_1$, C═O axial stretching appeared at 1595 $cm^{-1}$. For $Fe_3O_4/CS_{14}$ and $Fe_3O_4/CS_{34}$, C═O axial stretching and angular deformation of NH bonds shifted, respectively, to 1635 and 1540 $cm^{-1}$. For all types of $CS_{DA}$, SPIONs exhibited coupling of C−H angular deformation and C−N axial stretching at 1380 and 1420 $cm^{-1}$, the polysaccharide skeleton at 1065 $cm^{-1}$, and other bands for glycosidic bonds in the range of 1153−894 $cm^{-1}$. As a result, we conclude that significant interactions are formed between magnetite nanoparticles and CS chains, possibly through amine groups and acetyl groups for $CS_{14}$ and $CS_{34}$, respectively.

*3.1.3. Thermal Degradation of CS: Dosage and Interactions with Magnetite.* The obtained thermogravimetric analysis (TGA) results are listed in Table 1. Figure S4a shows the thermograms of CSs with different DAs ($CS_{DA}$). Mass losses below 200 °C are attributed to water desorption.[48] The degradation of CS started at 250 °C and was complete at 625 °C. No major differences were observed in the thermograms with the evolution of DA. Figure S4b shows the thermograms of uncoated and CS-coated SPIONs. Polymer degradations start at lower temperature in $CS_{DA}$/SPIONs in comparison to that in their pure CS references. Again, these changes are indicative of interactions between CS and the SPIONs' surface. On the noncoated $Fe_3O_4$ SPION curve, a slight mass increase of 0.5% was observed between 100 and 180 °C. This mass gain has been reported in several studies and is characteristic of magnetite.[49,50] It is due to the oxidation process of magnetite $Fe_3O_4$ to maghemite $\gamma$-$Fe_2O_3$. However, the theoretical mass gain for such conversion is 3.3%.[51] In our work, as in previously mentioned studies, it was found to be less than 1%. This is due to the overlap of two different processes, where the mass gain due to the oxidation of magnetite is superimposed with the elimination of OH groups and $H_2O$ molecules present at the SPIONs surface.

**Table 1. Structural Characteristics of the Synthesized Magnetite SPIONs[a]**

| samples | coating wt % | $d_{TEM}$ (nm) | $D_{WAXS}$ (nm) | $\varepsilon_{waxs}$ ($\times 10^{-4}$) | $d_{e,saxs}$ (nm) | $D_m$ (nm) |
|---|---|---|---|---|---|---|
| $Fe_3O_4$ | 0 | 9.6 | 9.7 | 0.3 | 13.1 | 9.5 |
| $Fe_3O_4/CS_1$ | 38.0 | 5.4 | 5.9 | −10.0 | 6.7 | 8.1 |
| $Fe_3O_4/CS_{14}$ | 38.8 | 5.7 | 5.2 | −9.0 | 6.7 | 7.5 |
| $Fe_3O_4/CS_{34}$ | 36.8 | 6.2 | 5.6 | −6.4 | 7.5 | 8.2 |

[a]Values $d_{TEM}$, $D_{WAXS}$, $d_{e,SAXS}$, and $D_m$ correspond to size of SPIONs measured using TEM, WAXS, SAXS, and VSM techniques, respectively.

The amount of coating on SPIONs was estimated by two different methods. In contact with air and above 250 °C, magnetite $Fe_3O_4$ tends to be oxidized in hematite $\alpha$-$Fe_2O_3\alpha - Fe_2O_3$,[51] following the reaction

$$4Fe_3O_4 + O_2 \rightarrow 6Fe_2O_3$$

In this study, thermograms were recorded under dry air flow, from 30 to 700 °C with a temperature rate of 10 °C/min. As the formation of hematite occurs at high temperature, it can be assumed that a complete conversion of $Fe_3O_4$ to $\alpha$-$Fe_2O_3$ was achieved at the end of thermal analyses at 700 °C. The first method relies on the hypothesis that the amount of iron remains constant through the entire TGA analysis and that the conversion of pure magnetite to hematite is characterized by a mass increase of 3.3%. Also, full degradation of the coatings was supposed at 700 °C, given the previous thermograms for CSs alone. Thus, a second method consists in measuring the mass loss associated with the complete degradation of CS, accounting again for the mass gain associated with magnetite to hematite conversion. Full calculations are available in SI5. Finally, both methods lead to comparable results, with a weight fraction of CS close to 38%. Logically, we obtained here higher weight percentages (wt %) of CS coatings than in our previous study with COS[37] (∼35−40% for CS coating in comparison with ∼10−15% for COS) even though the same protocol was applied and the same amount of iron salts and CS or COS were used. This is likely due to the higher molar mass of CS, contributing to a thicker coating in comparison to short COS.

In a second step, the amount of coating was varied, and two new batches of $CS_1$-coated SPIONs were synthesized. $CS_1$ was chosen for these tests as $Fe_3O_4/CS_1$ SPIONs showed the best results in MH experiments (see Section 3.3.2). For molar ratios $n_{CS1}/n_{Fe}$ of 0.3, 0.2, and 0.1 (see Section 2.2.4), results indicated coating mass fractions of 38, 29.6, and 19.3% w/w (of dry material), respectively, showing the possibility of tuning the coating amount on the SPIONs. This allows to find an optimal equilibrium between magnetic and biological properties (see Section 1). Therefore, with such CS coating, these two properties can be easily and precisely adjusted depending on the desired application. Figure S4c displays the thermograms for these experiments.

**3.2. Structural Characterizations of $Fe_3O_4$ and $Fe_3O_4/CS_{DA}$ SPIONs.** *3.2.1. Microscopic Analyses of SPION Dried Suspensions.* TEM experiments were performed to determine the size and the morphology of the SPIONs. Figure 1 shows the TEM images of SPIONs and the particle size histograms adjusted with a log−normal distribution.[52] All particles had a nearly spherical shape, with sizes ranging from 5 to 10 nm. The smallest sizes were obtained for CS-coated SPIONs, with an average size of 5.8 nm. Similar results were found in our previous study with $Fe_3O_4$ SPIONs coated with COSs.[36] This can be explained by the in situ method of synthesis of SPIONs, where CS is added to the solution of ferrous and ferric ions before the coprecipitation. CS may complex the iron ions at amino and hydroxyl sites.[53] Thus, such a complexation may promote dispersion and nucleation of SPIONs, reducing their size and narrowing their dispersity. The slight increase of SPIONs' size with DA of CS may be due to the less numerous amine groups as more amino complexation sites are substituted by acetyl groups when the DA increases. These results are in agreement with those we previously obtained with COS,[36] showing that the molar weight of CS should play a minor role


https://doi.org/10.1021/acsanm.3c06118
ACS Appl. Nano Mater. XXXX, XXX, XXX−XXX

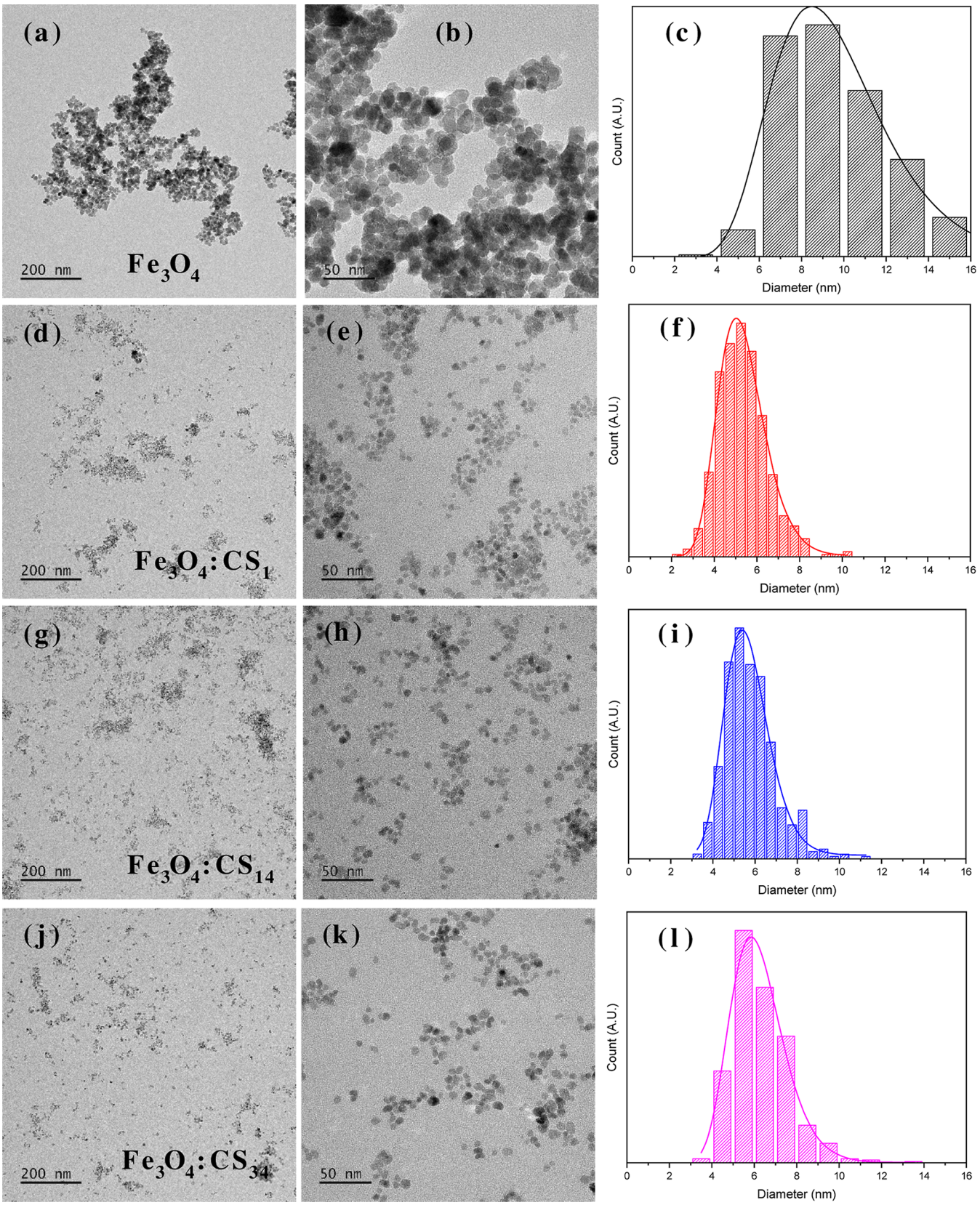


**Figure 1.** TEM pictures and histograms of size distribution profiles for (a–c) $Fe_3O_4$, the size distribution fitted with a log–normal distribution giving an average diameter $d_{TEM}$ = 9.6 ± 2.9 nm, (d–f) $Fe_3O_4/CS_1$, with $d_{TEM}$ = 5.4 ± 1.1 nm, (g–i) $Fe_3O_4/CS_{14}$, with $d_{TEM}$ = 5.7 ± 1.1 nm, (j–l) $Fe_3O_4/CS_{34}$, with $d_{TEM}$ = 6.2 ± 1.3 nm.

on the complexation and nucleation of magnetite nanoparticles.

TEM pictures also show aggregates of the SPIONs. As mentioned previously, this may be partly due to the large



https://doi.org/10.1021/acsanm.3c06118
ACS Appl. Nano Mater. XXXX, XXX, XXX–XXX

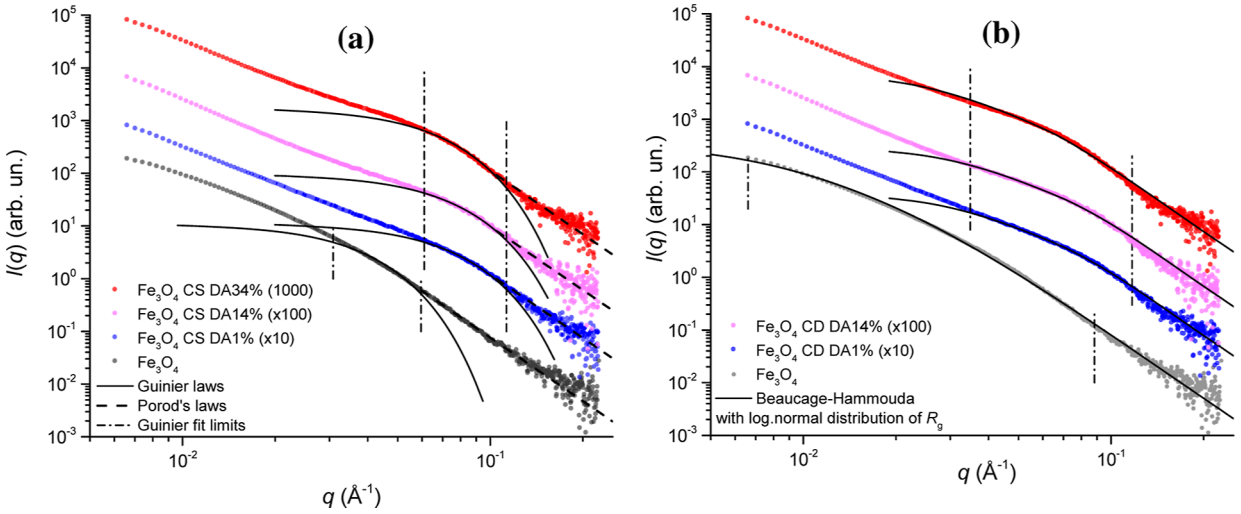


**Figure 2.** (a) SAXS diagrams showing experimental data and their modeling using the Guinier law for $Fe_3O_4$, $Fe_3O_4/CS_1$, $Fe_3O_4/CS_{14}$, and $Fe_3O_4/CS_{34}$ samples. The shoulder present in the coated systems is well reproduced, but the scattering of uncoated $Fe_3O_4$ nanoparticle suspension is poorly characterized as a result of a broader distribution of elementary particles. (b) Modeling of scattering data with a distribution of gyration radii evidencing the distribution of gyration radii in the noncoated $Fe_3O_4$ system.

surface/volume ratio of SPIONs, which leads to the formation of clusters to reduce the surface energy, but aggregation necessarily occurs after the drying of the SPION suspension, which was performed for TEM observations. Therefore, the aggregation state characterized by TEM pictures may not be representative of the aggregates present in suspension. CS-coated SPIONs appeared less aggregated than COS-coated ones,[36] possibly thanks to the steric hindrance effect enhanced by longer CS chains. It was not possible to clearly see the coatings on SPIONs, probably because of an insufficient contrast for CS compared to that for magnetite $Fe_3O_4$. However, given the single-crystal morphology of SPIONs, CS should not be inserted within the SPIONs' core but rather surround them and form a shell around the magnetite cores.

*3.2.2. Microstructural Study of SPIONs by SAXS.* The SAXS patterns of the $Fe_3O_4$ SPIONs are shown in Figure 2. For coated particles, we can divide the pattern in three domains. (i) In the low vector range ($q < 3 \times 10^{-2}$ Å$^{-1}$), scattering is dominated by the presence of aggregates of primary particles. Their analysis with the generalized Porod's law ($I(q) = Bq^{-\alpha}$) yields fractal exponents $\alpha \approx 2.3$ for all coated nanoparticles, typical of a rather compact aggregation of ultrafine particles.[54] Interestingly, this scattering behavior with an intensity upturn in the low $q$ range is not clearly found in the noncoated $Fe_3O_4$ nanoparticle system. This indicates that after freeze-drying, the coating may favor the formation of aggregates by chain interdiffusion and entangling, with such interparticle interactions remaining after redispersion with sonication in aqueous media and further dilution to 0.1 g/mL. (ii) In the intermediate scattering range, from $q = 5 \times 10^{-2}$ to 0.1 Å$^{-1}$, a shoulder is present on the scattering diagrams of the coated systems, which can be modeled with a Guinier law

$$I(q) = I_0 \exp\left(-\frac{R_g^2}{3}q^2\right) \quad (3)$$

(iii) In the $q$-range from 0.1 to 0.15 Å$^{-1}$, the Porod's regime is present as

$$I(q) = \frac{C}{q^4} \quad (4)$$

The results obtained for the gyration radii are displayed in SI6 and Table 1 as $d_{e,SAXS} = 2\sqrt{\frac{5}{3}}R_g$. Interestingly, the modeling of the uncoated $Fe_3O_4$ suspension may not reflect the actual distribution of gyration radii as the overlap between the Guinier model and the experimental data is limited to a rather restricted $q$-range, and no shoulder is clearly present on the scattering diagram. A more complex analysis was thus applied to the noncoated $Fe_3O_4$ nanoparticles to better account for a broader gyration radius distribution, as suggested by TEM observations. The scattering patterns were modeled accounting for a log−normal distribution of gyration radius of the particles, i.e., invoking a sum of Guinier and Porod laws, weighted by the distribution function $g(R_g)$. Hence, the scattered intensity can be theoretically written as

$$I(q, \mu, \sigma) = \int_0^{+\infty} k \cdot g(R_g) \cdot I_p(q) \cdot dR_g \quad (5)$$

where $I_p(q)$ can be written to combine the Guinier and Porod's laws[55]

$$I_p(q) = kR_g^6 \cdot \exp\left(-\frac{R_g^2 \cdot q^2}{3}\right) + \frac{C}{q^d}\left[\mathrm{erf}\left(\frac{qR_g}{\sqrt{6}}\right)\right]^{3d} \quad (6)$$

where $C = kR_g^{6-d}\left[\frac{6d^2}{(2+d)(2+2\times d)}\right]^{d/2}\Gamma\left(\frac{d}{2}\right)$

Hypothesizing a net interface of the $Fe_3O_4$ cores, $d = 4$ further results in $C = 10.24$ Å$^2$. $k$ is a scaling factor, $q = 4\pi\lambda^{-1}\sin(\theta)$, $2\theta$ is the Bragg angle, and $g(R_g)$ is the log−normal number distribution function of gyration radii $R_g$

$$g(R_g) = \frac{1}{R_g \cdot \sigma \cdot \sqrt{2\pi}} \exp\left(-\frac{(\ln(R_g) - \mu)^2}{2\sigma^2}\right) \quad (7)$$

where $R_g$ is the mean radius of gyration (Å).

The calculation of $I(q,\mu,\sigma)$ integral was performed by Lobatto's recursive adaptive quadrature, using the *quadl()*


https://doi.org/10.1021/acsanm.3c06118
ACS Appl. Nano Mater. XXXX, XXX, XXX−XXX

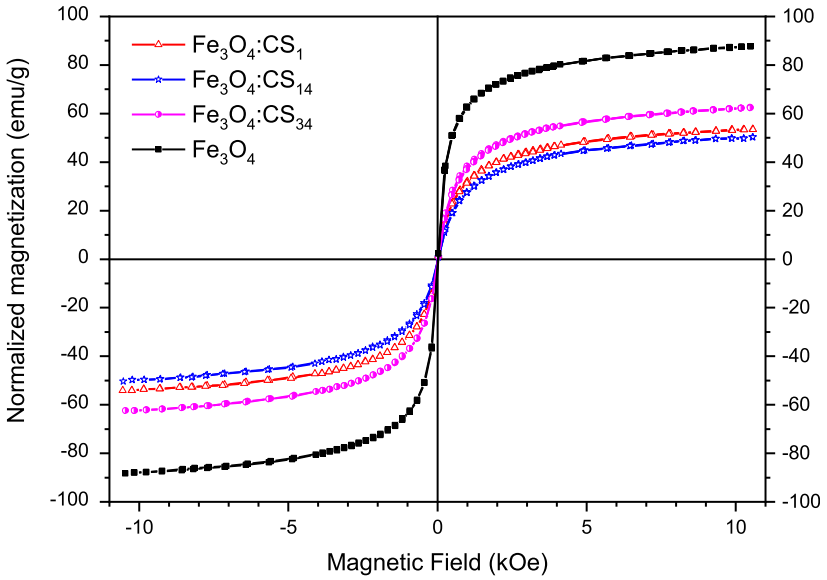


**Figure 3.** Normalized $M \times H$ curves (emu/g of $Fe_30_4$) for $Fe_3O_4$ and $Fe_3O_4/CS_{DA}$. CS coating decreases $M_S$ but does not impact coercivity.

function within Matlab or Octave environments, adapting the sampling of $R_g$ values in the relevant decades of the investigated $q$-range. Then, the determination of parameters $\mu$ and $\sigma$ was performed using the nonlinear least-squares solver *lsqcurvefit()*. The numerical results arising from the determination of the $g(R_g)$ distribution function shape parameters are shown in the bottom part of SI6. Such evaluation offers a way to deduce not only the number-average radius of gyration $M_1 = \langle R_g \rangle = e^{\mu+\sigma^2/2}$ but also all moments of the $g(R_g)$ distribution $M_k = \langle R_g^k \rangle = e^{k\mu+k^2\sigma^2/2}$ and their ratios. As shown in Figure 2 and SI6, the scattering curve of noncoated systems is well reproduced in the entire $q$-range with a rather broad distribution of particle gyration radii, with coefficient of variation $Cv = \sqrt{e^{\sigma^2} - 1} \approx 0.52$.

However, when the same distributed Beaucage−Hammouda analysis is applied on coated systems, a satisfactory modeling can only be obtained restricting the analyzed data to the $q$-range from $\sim 3.5 \times 10^{-2}$ to 0.12 $Å^{-1}$, thus excluding the large aggregate contribution, and choosing a generalized Porod exponent $d \sim 4.5$, indicative of the presence of a gradual decrease of electron density from the surface of the nanoparticles. In agreement with the TEM observations, the CS coatings induce a significant decrease of the mean gyration radius. A strong decrease of the breadth of the gyration radius distribution is reflected by very small values of parameter $\sigma$ and Cv. In fact, such negligible breadth parameters values may partly result from the restricted $q$-range used for the fits of the coated systems: it may not be possible to separate unambiguously the contribution of small aggregates of elementary particles and that of larger elementary particles.

As a general trend, comparing coated and noncoated SPIONs, CS coatings lead to a narrow distribution of particle sizes during the precipitation of magnetite nanoparticles, resulting in a net shoulder in the scattering patterns. However, it can also favor the formation of aggregates during freeze-drying of the suspension, the contribution of which was not taken into account in the TEM analysis of elementary particles.

*3.2.3. Crystalline Structure of Magnetite Cores Investigated by WAXS.* Figure S5 shows the diffraction diagrams (in transmission mode) obtained on SPION powders. The signal is largely dominated by the SPION $Fe_3O_4$ cores. The crystalline structure of the SPIONs can clearly be identified with several peaks corresponding to (111), (220), (311), (222), (400), (422), (511), (440) family of planes of magnetite. For $CS_{DA}$-coated SPIONs, a slight diffraction peak ($q \sim 1.42$ $Å^{-1}$) can be identified on each of the three spectra, showing the effective presence of CS on the surface of magnetite SPIONs. Larger diffraction peaks were observed for $CS_{DA}$-coated SPIONs. Such broadening can be induced both by size and strain.[56] In many works, the apparent crystallite sizes ($D_{WAXS}$) are calculated using Scherrer's equation, by considering the fwhm of the most intense (311) diffraction peak. However, this approach must be applied carefully as measuring crystallite size with a single diffraction peak only gives an information about the apparent dimension in one direction. Moreover, the Scherrer's equation does not consider the potential strain-induced peak broadening, and this may therefore lead to an underestimation or overestimation of crystallite size. Here, we chose to use the Williamson−Hall (WH) isotropic strain model for the analysis of peak broadening.[44] In this model, the lattice strain and the crystallite size are independent parameters, and the total peak broadening is calculated by adding the two contributions (see Section 2.3.6). The results are reported in Table 1. The WH plots as well as the results obtained using Scherrer's equation are shown in SI7. Interestingly, the obtained values with the WH model are very close to those measured by TEM, which indicates the monocrystalline structure of the SPIONs. Also, the tendency of CS to reduce the SPION size was also evidenced with these WAXS experiments. In addition, calculations of the apparent strain $\varepsilon$ from the WH model showed that the presence of coating is inducing a compression strain onto the cores (see Table 1, with negative strain values for $CS_{DA}$), unlike naked $Fe_3O_4$ SPIONs for which the strain is minimal. This compressive strain on cores of CS-coated SPIONs may be attributed to a complexation mechanism of surface $Fe^{3+}$ ions, partial oxidation of the surface of particles, and surface effects at the nanoscale. The strain values obtained here using the WH model can be found to be relatively small in comparison with those reported in other works in literature.[57]


https://doi.org/10.1021/acsanm.3c06118
ACS Appl. Nano Mater. XXXX, XXX, XXX−XXX

Table 2. Thermo-Magnetic Characteristics of Synthesized Magnetite SPIONs[a]

| samples | $M_s$ (emu/g) | SAR (W/g) | $r_1$ ($mM^{-1}$ $s^{-1}$) | $r_2$ ($mM^{-1}$ $s^{-1}$) | $r_2/r_1$ |
|---|---|---|---|---|---|
| $Fe_3O_4$ | 87.7 | 85.1 | 0.8 | 154 | 185 |
| $Fe_3O_4/CS_1$ (19.3 wt %) | | 83.0 | 0.7 | 127 | 177 |
| $Fe_3O_4/CS_1$ (29.6 wt %) | | 49.6 | 1.0 | 137 | 141 |
| $Fe_3O_4/CS_1$ (38.0 wt %) | 53.4 | 40.5 | 1.2 | 124 | 104 |
| $Fe_3O_4/CS_{14}$ (38.0 wt %) | 50.3 | 14.0 | 1.5 | 137 | 92 |
| $Fe_3O_4/CS_{34}$ (38.0 wt %) | 62.4 | 7.0 | 1.9 | 123 | 65 |

[a]Values of $r_1$,$r_2$, and $r_2/r_1$ are given at $B_0$ = 3 T. Values measured at other field strengths are given in SI12.

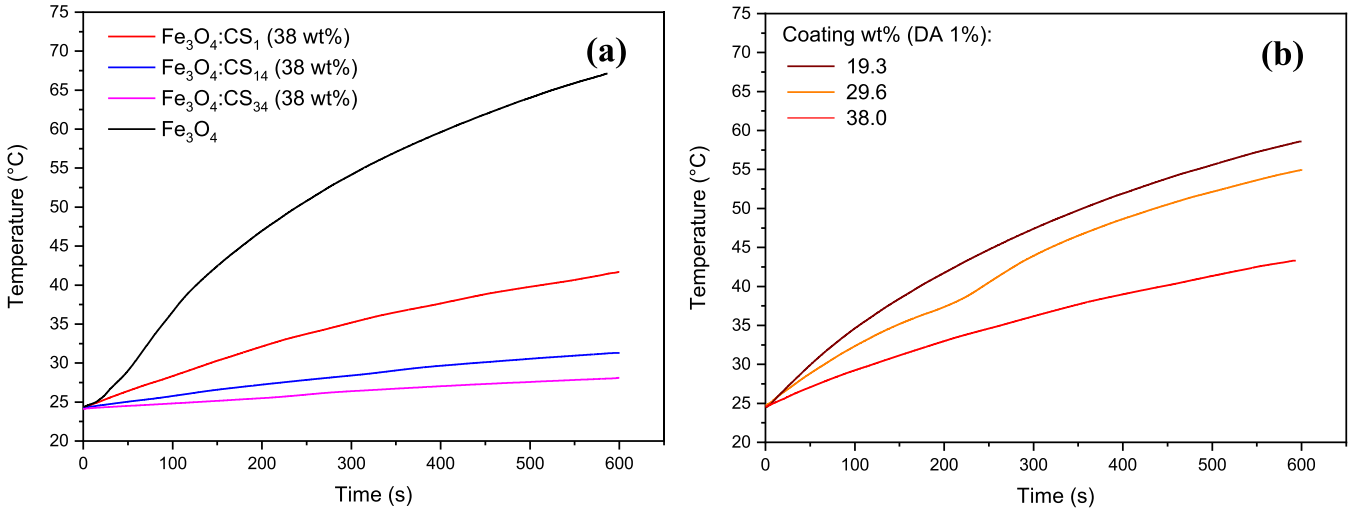


**Figure 4.** (a) Heating curves of $Fe_3O_4$, $Fe_3O_4/CS_1$, $Fe_3O_4/CS_{14}$, and $Fe_3O_4/CS_{34}$ SPIONs at a concentration of 5 mg/mL of $Fe_3O_4$, and a magnetic field amplitude and frequency of, respectively, 370 G and 491.45 kHz. (b) Heating curves of $Fe_3O_4/CS_1$ SPIONs with different amounts of coating, in the same experimental conditions.

However, it is known that the synthesis method is a key element contributing to residual microstrains in the samples.[57] Higher strains are more favored by mechanical and thermal processes than milder chemical syntheses. Our results stay in agreement with those of the studies in which the same synthesis protocols were used.[58,59]

**3.3. Magnetic Properties.** *3.3.1. Measurement of Magnetic Properties.* Figure 3 shows the $M$ (magnetization) vs $H$ (magnetic field) curves recorded at room temperature, normalized by the exact percentage of magnetite. The apparent magnetization at saturation ($M_S$) for noncoated $Fe_3O_4$ SPIONs was ~87 emu/g of nanoparticles, which is similar to values reported in the literature for bulk magnetite.[60] This result was not expected, since $M_S$ is usually lower for SPIONs than for the bulk material because of finite size effects (i.e., canting of the surface spins) and surface defects contributing to breaking of the crystal symmetry.[61] In this work, the decrease in $M_S$ also depended on the coating amount: the highest $M_S$ was reached for noncoated $Fe_3O_4$ SPIONs. It was lower for coated systems and measured to lie between ~50 and ~63 emu/g (coating representing 36.8−38.8 wt %) (see Table 2).

In order to exploit further the VSM curves, we used a modeling to separate the different components in the magnetization of the SPION nanoparticles. The magnetization for a single superparamagnetic nanoparticle can be classically expressed with the Langevin function $L(x)$[62]

$$M(H, T) = M_S \cdot L(x) + \chi H \quad (8)$$

where $L(x) = \coth(x) - \frac{1}{x}$, $x = \frac{\mu_p H}{k_B T}$, $\mu_p$ is the mean magnetic moment of the nanoparticle, $k_B$ the Boltzmann constant, $\chi$ the magnetic susceptibility, and $H$ the magnetic field. This modeling for $M(H,T)$ consists in two different contributions. The nonlinear Langevin term expresses the magnetization for an ideal superparamagnetic system, while the linear term characterizes the deviation to the Langevin behavior due to interparticle interactions, anisotropy, and inhomogeneities such as volume and moment distribution. Equation 8 was then used to fit the experimental VSM data. The results are shown in SI8. A good agreement was observed between the theoretical model and the experimental values. The two distinct Langevin and linear contributions were clearly evidenced. Interestingly, despite the size reduction of CS-coated SPIONs (see previous TEM, WAXS, and SAXS results), the linear contribution was found comparable to that of noncoated $Fe_3O_4$ SPIONs. It was also possible to extract the mean SPION diameters from the model using structural considerations to link the particle diameter to the mean magnetic moment $\mu_p$. The values of magnetic sizes are shown in Table 1. Briefly, magnetite crystallizes following an inverse spinel cubic structure with a unit cell volume $V_{UC}$ = 592.07 Å$^3$ containing $N$ = 8 formula units. The mean magnetic moment $\mu_p$, which was one of our fit parameters, can therefore be expressed by the equation $\mu_p = N \times mbfu \times P$, where $mbfu$ is the number of Bohr magneton per formula unit (which is 4.07 $\mu_B$ for bulk magnetite[61]) and $P$ the average number of unit cells in a single domain. The mean particle volume $V$ and so its


https://doi.org/10.1021/acsanm.3c06118
ACS Appl. Nano Mater. XXXX, XXX, XXX−XXX

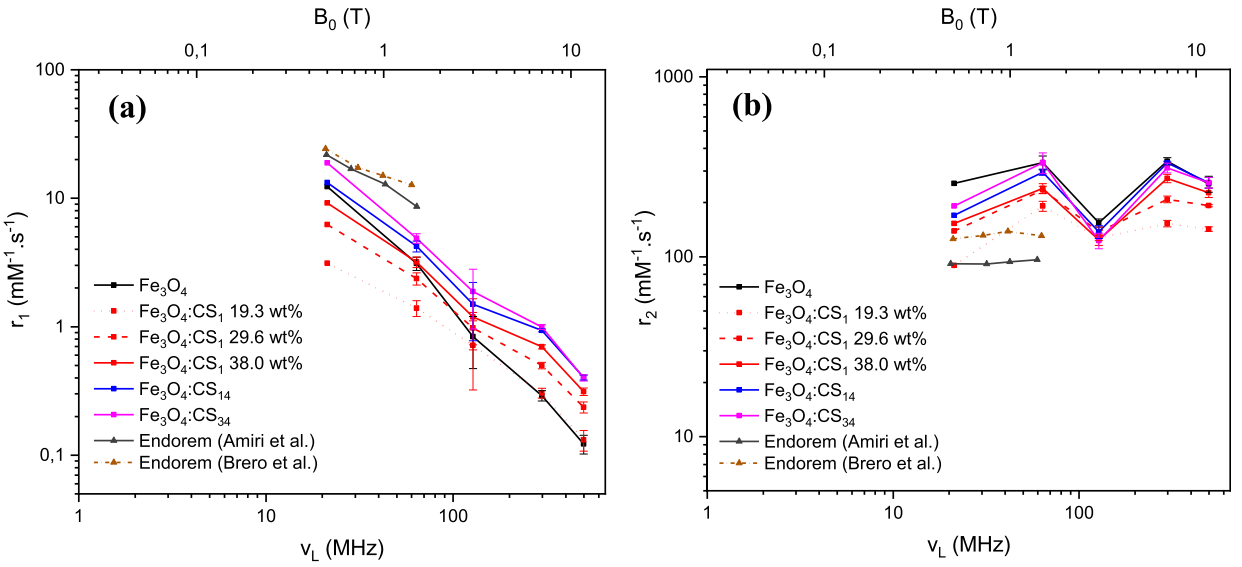


**Figure 5.** Evolution of $r_1$ (a) and $r_2$ (b) at different magnetic fields $B_0$ and Larmor frequencies $\nu_L$. Different systems synthesized in this work were analyzed at 0.02 and 0.05 g/L to deduce the relaxivities, and the results are compared with Endorem.[68,69]

diameter are therefore assessable by the relation $V = V_{UC} \times \mu_p / (N \times mbfu)$.

Finally, in the magnetic measurements as a function of temperature in the ZFC and FC regimes (see SI9), the samples showed a distinct irreversibility in a temperature known as the "blocking temperature" $T_B$. The $Fe_3O_4$ SPIONs presented a $T_B \sim 180$ K, and the CS-coated SPIONs show a $T_B \sim 125$ K. This corroborates the results presented previously and suggests a decrease in the magnetic interaction between the nanoparticles due to CS-coating. Therefore, we can conclude that at room temperature, the samples are in a superparamagnetic state.

*3.3.2. Characterization of Thermo-Magnetic Properties.* To evaluate the potential of the SPIONs for cancer treatment by MH, their magnetic heating (MH) abilities were studied at different field amplitudes and frequencies. The complete set of heating curves are available in SI10, and the corresponding temperature increases $\Delta T$, as shown in SI11. Figure 4a shows the heating curves of the different SPIONs in suspension at a $Fe_3O_4$ concentration of 5 mg/mL, for a field amplitude and frequency of, respectively, 370 G and 491,45 kHz. As expected, $\Delta T$ was higher for high magnetic fields and high frequencies. No resonance phenomena were observed. These results are in agreement with those of other studies conducted on different types of SPIONs.[63,64] Comparing our different systems, the characteristics of SPIONs impacted the MH efficacy. The highest $\Delta T$ values were obtained for noncoated $Fe_3O_4$ SPIONs, then a decrease was observed for $Fe_3O_4/CS_{DA}$ SPIONs. Finally, we investigated the evolution of MH properties with the amount of coating on SPIONs. Three batches of $Fe_3O_4/CS_1$ with 19, 29, and 38 wt % of $CS_1$ were compared, and the results are shown in Figure 4b. $\Delta T$ significantly increased for SPIONs with 19 and 29 wt % of $CS_1$ in comparison with SPIONs with 38 wt % of $CS_1$. These results showed that it is possible to tune MH properties to reach an optimal equilibrium between the need for a coating and the strength of the MH effect. We also observed that $\Delta T$ decreased with the DA of CS used as coating. This was more surprising and could not be explained by a difference of coating wt % as TGA showed that they were very similar (see Table 1). To the best of our knowledge, we could not find papers in literature treating this question. The explanation may reside in the physicochemical and structural properties of CS that change with the DA.

Even though $\Delta T$ obtained with MH testing could sharply vary with the type of SPIONs considered, it is worthy to note that many configurations investigated here could be suitable for MH. Indeed, MH requires the temperature of the zone of the treatment to be between 40 and 43 °C,[65,66] which means a temperature increase between 3 and 6 °C from the body temperature. Therefore, many of the tests performed in this work would satisfy this criterion (see SI11). To complete the analyses, we also calculated the SAR for each type of SPIONs. The SAR can be defined as the power absorbed per mass unit of the SPIONs. SI11 shows the SAR values for all MH experiments conducted. As for $\Delta T$, SAR increases with the amplitude and the frequency of the magnetic field. For noncoated $Fe_3O_4$ SPIONs, the SAR value measured at 491 kHz is multiplied by 12.2 within the amplitude range of 100−370 G. In the same way, the SAR value measured at 370 G is multiplied by 8.7 within the frequency range of 168−491 kHz. Regarding the different types of SPIONs, the highest SAR values are obtained for noncoated $Fe_3O_4$ SPIONs. This is in agreement with the evolution of $\Delta T$ and with other experiments conducted in this work, for which an increase of coating amount tends to decrease the magnetic properties as CS coating reduces the magnetic interaction between the SPIONs.

*3.3.3. Investigation of SPIONs as Contrast Agents for MRI.* $T_1$ and $T_2$ values at various static magnetic field $B_0$ (ranging from 0.5 to 11.7 T) were measured for all systems at two $Fe_3O_4$ concentrations (0.02 and 0.05 g/L, respectively, corresponding to iron concentrations $C$ = 0.259 and 0.648 mM), by combining measurements on several MR scanners. The data can be rationalized and compared with those from previous studies by the calculation of the relaxivities according to ref 67

$$r_i = \frac{\frac{1}{\mathrm{Ti}(C)} - \frac{1}{\mathrm{Ti}(C=0)}}{C} \qquad i = 1;\ 2 \tag{9}$$


https://doi.org/10.1021/acsanm.3c06118
ACS Appl. Nano Mater. XXXX, XXX, XXX−XXX

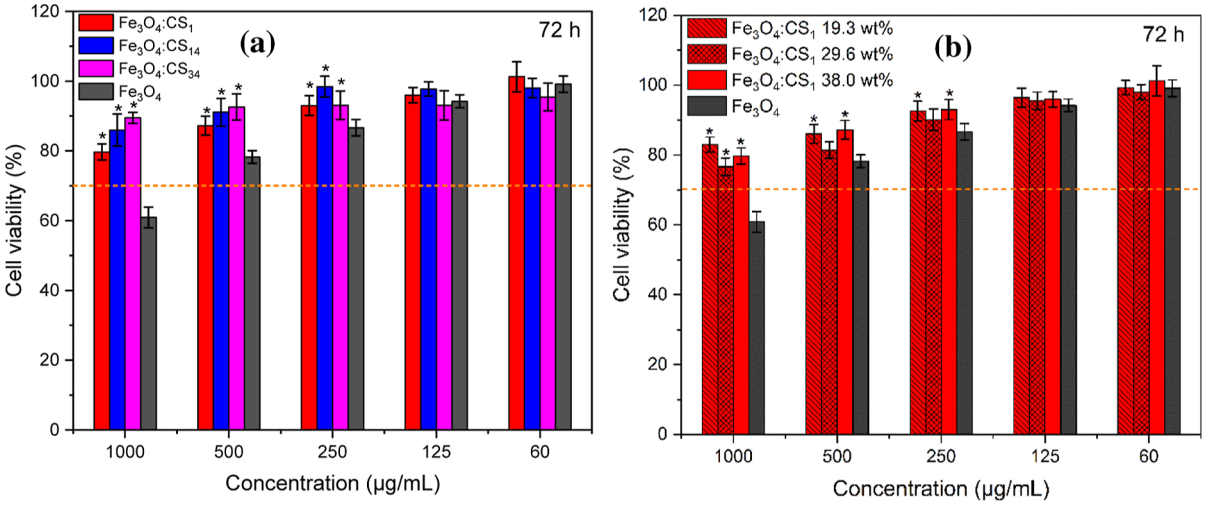


**Figure 6.** Cell viability results of canine fibroblasts after 72 h of interaction time against (a) $Fe_3O_4$ and $Fe_3O_4/CS_{DA}$ SPIONs at different concentrations with same amount of $CS_{DA}$ coating 38%, (b) $Fe_3O_4$ and $Fe_3O_4/CS_1$ at different concentrations and different amounts of $CS_1$ coating. * indicated statically different results of $Fe_3O_4/CS_{DA}$ from $Fe_3O_4$ SPIONs, using Tukey test and $p$ value < 0.05. Orange dashed line indicates threshold for cell viability, according to international standard procedure ISO 10993-5.

Figure 5 captures the evolution of $r_1$ and $r_2$ in comparison with published data for Endorem reference sample.[68,69] Interestingly, our $r_1$ values are lower, while we found higher $r_2$ values, evidencing the strongest efficacy of our systems for use as $T_2$ contrast agents. This strong $T_2$ high-field magnetic imaging performance is expressed by the ratio $r_2/r_1$, with values ranging from 65 to 185 at $B_0$ = 3 T (see Table 2). The complete set of data at different $B_0$ strengths is available in SI12. Regardless of the SPION type considered, the high-field magnetic imaging performance evaluated by the ratio $r_2/r_1$ (see Table 2) increases with the field strength. This is coherent with already reported results for other SPION types.[70] Interestingly, $r_2/r_1$ values were found to decrease with the coating amount for all SPION types. This tendency was similar for MH results (see Figure 4b), thus corroborating the idea that CS coating quantity directly lowers magnetic properties while keeping them satisfying. We also identified that $r_2/r_1$ is impacted by the DA of CS. Surprisingly, smaller DAs yield better imaging performance despite the strongest CS-Fe ions interactions through amine groups than with acetylated CS.

**3.4. Cytotoxicity Assay.** First, the SPIONs were observed with optical microscope after 24 h of contact with canine fibroblasts (see Figure S10). Different behaviors were found, depending on the formulation. As a general tendency, SPIONs were found aggregated in the culture medium. Aggregation was found stronger for the highest SPION concentration, and the dispersions were better for the low concentrations, with a better dispersion in the culture wells on both cellular layers and spaces without cells. Micrographs clearly showed that the presence of CS coating and the DA of CS had an influence on SPION aggregates, with larger aggregates forming at higher DAs. Also, an increase of coating mass fraction for DA = 1% appeared to favor the formation of aggregates. Overall, the spatial distribution of SPIONs in wells was heterogeneous. From these results, CS coating seemed to act as a sticking agent rather than a steric stabilizer (see SAXS results in Section 3.2.2). Moreover, SPIONs distributions seemed colocalized with cells. Indeed, no particles were observed in spaces without cells, while cellular layers were covered by SPIONs interacting with the cell surface or being internalized within fibroblasts.

SPIONs' cytotoxicity was assessed with CCK8 assays on canine fibroblasts after 24, 48, and 72 h of interaction. The data for 24 and 48 h are reported in SI13. As shown in Figure 6, cell viability increased with dilution of SPIONs. For concentrations of 125 μg/mL and below, viability was shown to be higher than 80% for all the formulations investigated and for the three interaction times. In the case of bare magnetite SPIONs, a toxicity was observed particularly at 24 and 72 h with a viability around 60% at a concentration of 1 mg/mL. The addition of a CS coating apparently decreased this toxicity (viability >80%), regardless of the DA and of the amount of CS coating. Therefore, we suggest that the thinnest CS coating layers onto the magnetite SPIONs are enough to preserve the biocompatibility of such systems while maintaining strong magnetic properties and minimizing their aggregation (see Figure S10). However, such results have to be interpreted carefully as SPION aggregation in culture medium causes a heterogeneous spatial distribution of the nanoparticles, which may affect cell viability in different ways: first, aggregates may be more difficult to internalize, possibly introducing a bias in the evaluation of their intrinsic cytocompatibility; second, in the form of aggregates, fibroblasts may not be in contact at all with primary SPIONs. Therefore, we consider such results as encouraging, and further efforts will be made to obtain well dispersed systems even for highest coating amounts, in order to study the impact of SPION aggregation.

Altogether, these results tend to show that the CS coating improved biocompatibility of magnetite-based SPIONs. $Fe_3O_4/CS_{DA}$ systems are thus fully compatible with the standard international procedure "Tests for in vitro cytotoxicity" ISO 10993-5 for all tested concentrations and interaction times, while bare $Fe_3O_4$ systems exhibit some toxicity at high concentrations (above 500 μg/mL).

Finally, most of the results obtained in this work were in qualitative agreement with those obtained previously with CS oligomers, which are more difficult to synthesize. Therefore, both options may be suitable for designing biocompatible SPIONs. Further improvements may focus on the development of an efficient method to prevent or control the aggregation of CS-coated SPIONs.


https://doi.org/10.1021/acsanm.3c06118
ACS Appl. Nano Mater. XXXX, XXX, XXX−XXX

## 4. CONCLUSIONS

We successfully synthesized and fully characterized $Fe_3O_4$ magnetite SPIONs coated with well characterized and comparable CSs, using a simple coprecipitation method without the use of any organic solvent within CS solutions. The SPIONs obtained were spherical and had a size between 5 and 10 nm, and the presence of highly crystalline magnetite phase was clearly evidenced by WAXS analyses. TGA analyses showed that CS coating amounts onto magnetite cores could be easily and precisely adjusted, playing on the initial concentration of CS in the precipitation medium. The presence of a coating impacted the magnetic properties ($M_S$, SAR, $r_2$), which decreased with coating addition, while the biological properties were improved by the presence of CS coating but remained independent of its quantity and DA in the investigated mass fraction range. Also, the impact of CS DAs on both property types was investigated. Higher DAs tended to decrease MRI and hyperthermia efficacy, while SAXS analyses and optical microscopy observations revealed that they promoted aggregation. Therefore, we suggest that optimal CS-coated SPIONs would result from the addition of a thin shell (20%) of low DA (1%) CS in order to strengthen biocompatibility while maintaining excellent magnetic properties. We believe that such SPIONs will find applications in the fields of MRI, MH, and magnetic field-assisted drug delivery, among others.

## ■ ASSOCIATED CONTENT

### Supporting Information

The Supporting Information is available free of charge at https://pubs.acs.org/doi/10.1021/acsanm.3c06118.

CSs characterization by SEC and $^1$H NMR, FTIR spectra, TGA graphs, TGA and SAXS calculation details, WAXS diffraction profiles, WH plots, magnetization curves, FC-ZFC curves, *MH* curves, SAR values, MRI data, and cytotoxicity assay results at 24, 48, and 72 h (PDF)

## ■ AUTHOR INFORMATION


### Corresponding Authors

**Paula Nunes De Oliveira** − *Universite Claude Bernard Lyon 1, INSA de Lyon, Universite Jean Monnet St Etienne, CNRS, Ingénierie des Matériaux Polymères (IMP) UMR 5223, Villeurbanne F-69100, France*; Email: paulaoliveiraqmc@gmail.com

**Laurent David** − *Universite Claude Bernard Lyon 1, INSA de Lyon, Universite Jean Monnet St Etienne, CNRS, Ingénierie des Matériaux Polymères (IMP) UMR 5223, Villeurbanne F-69100, France*; orcid.org/0000-0003-3632-8537; Email: laurent.david@univ-lyon1.fr

### Authors

**Jules Mistral** − *Universite Claude Bernard Lyon 1, INSA de Lyon, Universite Jean Monnet St Etienne, CNRS, Ingénierie des Matériaux Polymères (IMP) UMR 5223, Villeurbanne F-69100, France*; orcid.org/0000-0002-5125-3556

**Kevin Tse Ve Koon** − *Universite Claude Bernard Lyon 1, INSA de Lyon, CNRSRINGGOLD, CREATIS, UMR 5223, INSERM U1294, Villeurbanne F-69100, France*; orcid.org/0000-0001-9780-8337

**Luiz Fernando Cotica** − *Department of Physics, State University of Maringá, Maringá, Paraña 87020-900, Brazil*; orcid.org/0000-0003-2634-447X

**Gustavo Sanguino Dias** − *Department of Physics, State University of Maringá, Maringá, Paraña 87020-900, Brazil*; orcid.org/0000-0001-8548-1146

**Ivair Aparecido Santos** − *Department of Physics, State University of Maringá, Maringá, Paraña 87020-900, Brazil*; orcid.org/0000-0001-7775-0692

**Pierre Alcouffe** − *Universite Claude Bernard Lyon 1, INSA de Lyon, Universite Jean Monnet St Etienne, CNRS, Ingénierie des Matériaux Polymères (IMP) UMR 5223, Villeurbanne F-69100, France*

**Nadège Milhau** − *UPSP 2016.A104 Interactions Cellules Environement, Veterinary School of Lyon (VetAgro Sup), Marcy l'Etoile F-69280, France*

**Didier Pin** − *UPSP 2016.A104 Interactions Cellules Environement, Veterinary School of Lyon (VetAgro Sup), Marcy l'Etoile F-69280, France*; orcid.org/0000-0001-7424-0013

**Olivier Chapet** − *Department of Radiation Oncology, Centre Hospitalier Lyon-Sud, Pierre-Bénite F-69310, France*; orcid.org/0000-0003-0347-8598

**Anatoli Serghei** − *Universite Claude Bernard Lyon 1, INSA de Lyon, Universite Jean Monnet St Etienne, CNRS, Ingénierie des Matériaux Polymères (IMP) UMR 5223, Villeurbanne F-69100, France*; orcid.org/0000-0002-6656-850X

**Guillaume Sudre** − *Universite Claude Bernard Lyon 1, INSA de Lyon, Universite Jean Monnet St Etienne, CNRS, Ingénierie des Matériaux Polymères (IMP) UMR 5223, Villeurbanne F-69100, France*; orcid.org/0000-0003-3545-7046

**Catherine Ladavière** − *Universite Claude Bernard Lyon 1, INSA de Lyon, Universite Jean Monnet St Etienne, CNRS, Ingénierie des Matériaux Polymères (IMP) UMR 5223, Villeurbanne F-69100, France*; orcid.org/0000-0002-6039-7471

Complete contact information is available at: https://pubs.acs.org/10.1021/acsanm.3c06118


### Notes

The authors declare no competing financial interest.

## ■ ACKNOWLEDGMENTS

This work was funded by Elekta (Sweden) under a consortium agreement with Université Claude Bernard Lyon 1, Hospices civils de Lyon (HCL) and Veterinary School of Lyon (VetAgro Sup).

## ■ REFERENCES

(1) Price, P. M.; Mahmoud, W. E.; Al-Ghamdi, A. A.; Bronstein, L. M. Magnetic Drug Delivery: Where the Field Is Going. *Front. Chem.* **2018**, *6*, 619.

(2) Niculaes, D.; Lak, A.; Anyfantis, G. C.; Marras, S.; Laslett, O.; Avugadda, S. K.; Cassani, M.; Serantes, D.; Hovorka, O.; Chantrell, R.; et al. Asymmetric Assembling of Iron Oxide Nanocubes for Improving Magnetic Hyperthermia Performance. *ACS Nano* **2017**, *11* (12), 12121−12133.

(3) Stephen, Z. R.; Kievit, F. M.; Zhang, M. Magnetite Nanoparticles for Medical MR Imaging. *Mater. Today* **2011**, *14* (7−8), 330−338.

(4) Chen, D.; Tang, Q.; Li, X.; Zhou, X.; Zang, J.; Xiang, J. y.; Guo, C. q.; Guo, C. Q. Biocompatibility of magnetic Fe3O4 nanoparticles

and their cytotoxic effect on MCF-7 cells. *Int. J. Nanomed.* **2012**, *7*, 4973−4982.
(5) Wu, W.; Wu, Z.; Yu, T.; Jiang, C.; Kim, W. S. Recent progress on magnetic iron oxide nanoparticles: synthesis, surface functional strategies and biomedical applications. *Sci. Technol. Adv. Mater.* **2015**, *16* (2), 023501.
(6) Li, Q.; Kartikowati, C. W.; Horie, S.; Ogi, T.; Iwaki, T.; Okuyama, K. Correlation between particle size/domain structure and magnetic properties of highly crystalline Fe3O4 nanoparticles. *Sci. Rep.* **2017**, *7* (1), 9894.
(7) Gavilán, H.; Posth, O.; Bogart, L. K.; Steinhoff, U.; Gutiérrez, L.; Morales, M. P. How shape and internal structure affect the magnetic properties of anisometric magnetite nanoparticles. *Acta Mater.* **2017**, *125*, 416−424.
(8) Belanova, A. A.; Gavalas, N.; Makarenko, Y. M.; Belousova, M. M.; Soldatov, A. V.; Zolotukhin, P. V. Physicochemical Properties of Magnetic Nanoparticles: Implications for Biomedical Applications In Vitro and In Vivo. *Oncol. Res. Treat.* **2018**, *41* (3), 139−143.
(9) Xu, C.; Sun, S. New forms of superparamagnetic nanoparticles for biomedical applications. *Adv. Drug Deliv. Rev.* **2013**, *65* (5), 732−743.
(10) Ali, A.; Zafar, H.; Zia, M.; Ul Haq, I.; Phull, A. R.; Ali, J. S.; Hussain, A. Synthesis, characterization, applications, and challenges of iron oxide nanoparticles. *Nanotechnol. Sci. Appl.* **2016**, *9*, 49−67.
(11) Massart, R. Preparation of aqueous magnetic liquids in alkaline and acidic media. *IEEE Trans. Magn.* **1981**, *17* (2), 1247−1248.
(12) Liu, G.; Gao, J.; Ai, H.; Chen, X. Applications and potential toxicity of magnetic iron oxide nanoparticles. *Small* **2013**, *9* (9−10), 1533−1545.
(13) Mahmoudi, M.; Simchi, A.; Milani, A. S.; Stroeve, P. Cell toxicity of superparamagnetic iron oxide nanoparticles. *J. Colloid Interface Sci.* **2009**, *336* (2), 510−518.
(14) Feng, Q.; Liu, Y.; Huang, J.; Chen, K.; Huang, J.; Xiao, K. Uptake, distribution, clearance, and toxicity of iron oxide nanoparticles with different sizes and coatings. *Sci. Rep.* **2018**, *8* (1), 2082.
(15) Ioţa, M.-A.; Cursaru, L.-M.; Şchiopu, A.-G.; Tudor, I. A.; Motoc, A.-M.; Piticescu, R. M. Fe3O4 Core−Shell Nanostructures with Anticancer and Antibacterial Properties: A Mini-Review. *Processes* **2023**, *11*, 1882.
(16) Mandal, M.; Kundu, S.; Ghosh, S. K.; Panigrahi, S.; Sau, T. K.; Yusuf, S. M.; Pal, T. Magnetite nanoparticles with tunable gold or silver shell. *J. Colloid Interface Sci.* **2005**, *286* (1), 187−194.
(17) Sabale, S.; Kandesar, P.; Jadhav, V.; Komorek, R.; Motkuri, R. K.; Yu, X.-Y. Recent developments in the synthesis, properties, and biomedical applications of core/shell superparamagnetic iron oxide nanoparticles with gold. *Biomater. Sci.* **2017**, *5* (11), 2212−2225.
(18) Gupta, J.; Hassan, P. A.; Barick, K. C. Core-shell Fe3O4@ZnO nanoparticles for magnetic hyperthermia and bio-imaging applications. *AIP Adv.* **2021**, *11* (2), 025207.
(19) Khashan, S.; Dagher, S.; Tit, N.; Alazzam, A.; Obaidat, I. Novel method for synthesis of Fe3O4@TiO2 core/shell nanoparticles. *Surf. Coat. Technol.* **2017**, *322*, 92−98.
(20) Santra, S.; Tapec, R.; Theodoropoulou, N.; Dobson, J.; Hebard, A.; Tan, W. Synthesis and Characterization of Silica-Coated Iron Oxide Nanoparticles in Microemulsion: The Effect of Nonionic Surfactants. *Langmuir* **2001**, *17* (10), 2900−2906.
(21) Le, T. T. H.; Bui, T. Q.; Ha, T. M. T.; Le, M. H.; Pham, H. N.; Ha, P. T. Optimizing the alginate coating layer of doxorubicin-loaded iron oxide nanoparticles for cancer hyperthermia and chemotherapy. *J. Mater. Sci.* **2018**, *53* (19), 13826−13842.
(22) Tassa, C.; Shaw, S. Y.; Weissleder, R. Dextran-coated iron oxide nanoparticles: a versatile platform for targeted molecular imaging, molecular diagnostics, and therapy. *Acc. Chem. Res.* **2011**, *44* (10), 842−852.
(23) Anbarasu, M.; Anandan, M.; Chinnasamy, E.; Gopinath, V.; Balamurugan, K. Synthesis and characterization of polyethylene glycol (PEG) coated Fe3O4 nanoparticles by chemical co-precipitation method for biomedical applications. *Spectrochim. Acta, Part A* **2015**, *135*, 536−539.
(24) Wáng, Y. X. J.; Idée, J. M. A comprehensive literature update of clinical researches of superparamagnetic resonance iron oxide nanoparticles for magnetic resonance imaging. *Quant. Imag. Med. Surg.* **2017**, *7* (1), 88−122.
(25) Dadfar, S. M.; Roemhild, K.; Drude, N. I.; von Stillfried, S.; Knüchel, R.; Kiessling, F.; Lammers, T. Iron oxide nanoparticles: Diagnostic, therapeutic and theranostic applications. *Adv. Drug Deliv. Rev.* **2019**, *138*, 302−325.
(26) Singh, P.; Upadhyay, C. Role of silver nanoshells on structural and magnetic behavior of Fe3O4 nanoparticles. *J. Magn. Magn. Mater.* **2018**, *458*, 39−47.
(27) de Mendonça, E. S. D. T.; de Faria, A. C. B.; Dias, S. C. L.; Aragón, F. F.; Mantilla, J. C.; Coaquira, J. A. H.; Dias, J. A. Effects of silica coating on the magnetic properties of magnetite nanoparticles. *Surface. Interfac.* **2019**, *14*, 34−43.
(28) Khalkhali, M.; Rostamizadeh, K.; Sadighian, S.; Khoeini, F.; Naghibi, M.; Hamidi, M. The impact of polymer coatings on magnetite nanoparticles performance as MRI contrast agents: a comparative study. *Daru* **2015**, *23* (1), 45.
(29) Soares, P. I. P.; Machado, D.; Laia, C.; Pereira, L. C. J.; Coutinho, J. T.; Ferreira, I. M. M.; Novo, C. M. M.; Borges, J. P. Thermal and magnetic properties of chitosan-iron oxide nanoparticles. *Carbohydr. Polym.* **2016**, *149*, 382−390.
(30) Pham, X. N.; Nguyen, T. P.; Pham, T. N.; Tran, T. T. N.; Tran, T. V. T. Synthesis and characterization of chitosan-coated magnetite nanoparticles and their application in curcumin drug delivery. *Adv. Nat. Sci.* **2016**, *7*, 045010.
(31) Unsoy, G.; Yalcin, S.; Khodadust, R.; Gunduz, G.; Gunduz, U. Synthesis optimization and characterization of chitosan-coated iron oxide nanoparticles produced for biomedical applications. *J. Nanopart. Res.* **2012**, *14* (11), 964.
(32) Arami, H.; Stephen, Z.; Veiseh, O.; Zhang, M. Chitosan-Coated Iron Oxide Nanoparticles for Molecular Imaging and Drug Delivery. In *Chitosan for Biomaterials I*; Jayakumar, R., Prabaharan, M., Muzzarelli, R. A. A., Eds.; Springer Berlin Heidelberg, 2011; pp 163−184.
(33) Ravi Kumar, M. N. V. A review of chitin and chitosan applications. *React. Funct. Polym.* **2000**, *46* (1), 1−27.
(34) Hassani, S.; Gharehaghaji, N.; Divband, B. Chitosan-coated iron oxide/graphene quantum dots as a potential multifunctional nanohybrid for bimodal magnetic resonance/fluorescence imaging and 5-fluorouracil delivery. *Mater. Today Commun.* **2022**, *31*, 103589.
(35) Gómez Pérez, A.; González-Martínez, E.; Díaz Águila, C. R.; González-Martínez, D. A.; González Ruiz, G.; García Artalejo, A.; Yee-Madeira, H. Chitosan-coated magnetic iron oxide nanoparticles for DNA and rhEGF separation. *Colloids Surf., A* **2020**, *591*, 124500.
(36) de Oliveira, P. N.; Moussa, A.; Milhau, N.; Dosciatti Bini, R.; Prouillac, C.; Ferraz de Oliveira, B.; Dias, G. S.; Santos, I. A.; Morfin, I.; Sudre, G.; et al. In situ synthesis of Fe(3)O(4) nanoparticles coated by chito-oligosaccharides: physico-chemical characterizations and cytotoxicity evaluation for biomedical applications. *Nanotechnology* **2020**, *31* (17), 175602.
(37) Hirai, A.; Odani, H.; Nakajima, A. Determination of degree of deacetylation of chitosan by 1H NMR spectroscopy. *Polym. Bull.* **1991**, *26* (1), 87−94.
(38) Schatz, C.; Viton, C.; Delair, T.; Pichot, C.; Domard, A. Typical Physicochemical Behaviors of Chitosan in Aqueous Solution. *Biomacromolecules* **2003**, *4* (3), 641−648.
(39) Wu, D.; Delair, T. Stabilization of chitosan/hyaluronan colloidal polyelectrolyte complexes in physiological conditions. *Carbohydr. Polym.* **2015**, *119*, 149−158.
(40) Lamarque, G.; Lucas, J.-M.; Viton, C.; Domard, A. Physicochemical Behavior of Homogeneous Series of Acetylated Chitosans in Aqueous Solution: Role of Various Structural Parameters. *Biomacromolecules* **2005**, *6* (1), 131−142.
(41) Vachoud, L.; Zydowicz, N.; Domard, A. Formation and characterisation of a physical chitin gel. *Carbohydr. Res.* **1997**, *302* (3−4), 169−177.


https://doi.org/10.1021/acsanm.3c06118
ACS Appl. Nano Mater. XXXX, XXX, XXX−XXX

(42) Estévez, M.; Cicuéndez, M.; Crespo, J.; Serrano-López, J.; Colilla, M.; Fernández-Acevedo, C.; Oroz-Mateo, T.; Rada-Leza, A.; González, B.; Izquierdo-Barba, I.; et al. Large-scale production of superparamagnetic iron oxide nanoparticles by flame spray pyrolysis: In vitro biological evaluation for biomedical applications. *J. Colloid Interface Sci.* **2023**, *650*, 560−572.
(43) Chahine, G. A.; Blanc, N.; Arnaud, S.; De Geuser, F.; Guinebretière, R.; Boudet, N. Advanced Non-Destructive in Situ Characterization of Metals with the French Collaborating Research Group D2AM/BM02 Beamline at the European Synchrotron Radiation Facility. *Metals* **2019**, *9*, 352.
(44) Williamson, G. K.; Hall, W. H. X-ray line broadening from filed aluminium and wolfram. *Acta Metall.* **1953**, *1* (1), 22−31.
(45) Kumirska, J.; Czerwicka, M.; Kaczyński, Z.; Bychowska, A.; Brzozowski, K.; Thöming, J.; Stepnowski, P. Application of spectroscopic methods for structural analysis of chitin and chitosan. *Mar. Drugs* **2010**, *8* (5), 1567−1636.
(46) Pawlak, A.; Mucha, M. Thermogravimetric and FTIR studies of chitosan blends. *Thermochim. Acta* **2003**, *396* (1−2), 153−166.
(47) Waldron, R. D. Infrared Spectra of Ferrites. *Phys. Rev.* **1955**, *99* (6), 1727−1735.
(48) Lesiak, B.; Rangam, N.; Jiricek, P.; Gordeev, I.; Tóth, J.; Kövér, L.; Mohai, M.; Borowicz, P. Surface Study of Fe(3)O(4) Nanoparticles Functionalized With Biocompatible Adsorbed Molecules. *Front. Chem.* **2019**, *7*, 642.
(49) Stoia, M.; Istratie, R.; Păcurariu, C. Investigation of magnetite nanoparticles stability in air by thermal analysis and FTIR spectroscopy. *J. Therm. Anal. Calorim.* **2016**, *125* (3), 1185−1198.
(50) Daou, T. J.; Pourroy, G.; Bégin-Colin, S.; Grenèche, J. M.; Ulhaq-Bouillet, C.; Legaré, P.; Bernhardt, P.; Leuvrey, C.; Rogez, G. Hydrothermal Synthesis of Monodisperse Magnetite Nanoparticles. *Chem. Mater.* **2006**, *18* (18), 4399−4404.
(51) Monazam, E. R.; Breault, R. W.; Siriwardane, R. Kinetics of Magnetite (Fe3O4) Oxidation to Hematite (Fe2O3) in Air for Chemical Looping Combustion. *Ind. Eng. Chem. Res.* **2014**, *53* (34), 13320−13328.
(52) Kiss, L. B.; Söderlund, J.; Niklasson, G. A.; Granqvist, C. G. New approach to the origin of lognormal size distributions of nanoparticles. *Nanotechnology* **1999**, *10* (1), 25−28.
(53) Farinelli, G.; Di Luca, A.; Kaila, V. R. I.; MacLachlan, M. J.; Tiraferri, A. Fe-chitosan complexes for oxidative degradation of emerging contaminants in water: Structure, activity, and reaction mechanism. *J. Hazard. Mater.* **2021**, *408*, 124662.
(54) Liao, J. Y. H.; Selomulya, C.; Bushell, G.; Bickert, G.; Amal, R. On Different Approaches to Estimate the Mass Fractal Dimension of Coal Aggregates. *Part. Part. Syst. Char.* **2005**, *22* (5), 299−309.
(55) Hammouda, B. A new Guinier-Porod model. *J. Appl. Crystallogr.* **2010**, *43* (4), 716−719.
(56) Burton, A. W.; Ong, K.; Rea, T.; Chan, I. Y. On the estimation of average crystallite size of zeolites from the Scherrer equation: A critical evaluation of its application to zeolites with one-dimensional pore systems. *Microporous Mesoporous Mater.* **2009**, *117* (1−2), 75−90.
(57) Vives, S.; Gaffet, E.; Meunier, C. X-ray diffraction line profile analysis of iron ball milled powders. *J. Mater. Sci. Eng. A* **2004**, *366* (2), 229−238.
(58) Jafari, A.; Farjami Shayesteh, S.; Salouti, M.; Boustani, K. Dependence of structural phase transition and lattice strain of Fe3O4 nanoparticles on calcination temperature. *Indian J. Phys.* **2015**, *89* (6), 551−560.
(59) Yusoff, A. H. M.; Salimi, M. N.; Jamlos, M. F. Dependence of lattice strain of magnetite nanoparticles on precipitation temperature and pH of solution. *J. Phys.: Conf. Ser.* **2017**, *908* (1), 012065.
(60) Cornell, R. M.; Schwertmann, U. *The Iron Oxides: Structure, Properties, Reactions, Occurrences, and Uses*; Wiley VCH: Weinheim, 2003.
(61) Cótica, L. F.; Santos, I. A.; Girotto, E. M.; Ferri, E. V.; Coelho, A. A. Surface spin disorder effects in magnetite and poly(thiophene)-coated magnetite nanoparticles. *J. Appl. Phys.* **2010**, *108* (6), 064325.
(62) Makhlouf, S. A.; Parker, F. T.; Berkowitz, A. E. Magnetic hysteresis anomalies in ferritin. *Phys. Rev. B* **1997**, *55* (22), R14717−R14720.
(63) Rego, G. N. d. A.; Mamani, J. B.; Souza, T. K. F.; Nucci, M. P.; Silva, H. R. D.; Gamarra, L. F. Therapeutic evaluation of magnetic hyperthermia using Fe3O4-aminosilane-coated iron oxide nanoparticles in glioblastoma animal model. *Einstein* **2019**, *17* (4), No. eAO4786.
(64) Ghosh, R.; Pradhan, L.; Devi, Y. P.; Meena, S. S.; Tewari, R.; Kumar, A.; Sharma, S.; Gajbhiye, N. S.; Vatsa, R. K.; Pandey, B. N.; et al. Induction heating studies of Fe3O4 magnetic nanoparticles capped with oleic acid and polyethylene glycol for hyperthermia. *J. Mater. Chem.* **2011**, *21* (35), 13388−13398.
(65) Hildebrandt, B.; Wust, P.; Ahlers, O.; Dieing, A.; Sreenivasa, G.; Kerner, T.; Felix, R.; Riess, H. The cellular and molecular basis of hyperthermia. *Criti. Rev. Oncol. Hemat.* **2002**, *43* (1), 33−56.
(66) Spirou, S. V.; Basini, M.; Lascialfari, A.; Sangregorio, C.; Innocenti, C. Magnetic Hyperthermia and Radiation Therapy: Radiobiological Principles and Current Practice (†). *Nanomaterials* **2018**, *8* (6), 401.
(67) Busquets, M. A.; Estelrich, J.; Sánchez-Martín, M. J. Nanoparticles in magnetic resonance imaging: from simple to dual contrast agents. *Int. J. Nanomed.* **2015**, *10*, 1727−1741.
(68) Amiri, H.; Bordonali, L.; Lascialfari, A.; Wan, S.; Monopoli, M.; Lynch, I.; Laurent, S.; Mahmoudi, M. Protein corona affects the relaxivity and MRI contrast efficiency of magnetic nanoparticles. *Nanoscale* **2013**, *5*, 8656.
(69) Brero, F.; Basini, M.; Avolio, M.; Orsini, F.; Arosio, P.; Sangregorio, C.; Innocenti, C.; Guerrini, A.; Boucard, J.; Ishow, E.; et al. Coating Effect on the (1)H-NMR Relaxation Properties of Iron Oxide Magnetic Nanoparticles. *Nanomaterials* **2020**, *10* (9), 1660.
(70) Jedlovszky-Hajdú, A.; Tombácz, E.; Bányai, I.; Babos, M.; Palkó, A. Carboxylated magnetic nanoparticles as MRI contrast agents: Relaxation measurements at different field strengths. *J. Magn. Magn. Mater.* **2012**, *324* (19), 3173−3180.


https://doi.org/10.1021/acsanm.3c06118
*ACS Appl. Nano Mater.* XXXX, XXX, XXX−XXX